ChemPubSoc Europe

DOI: 10.1002/cphc.201900714

CHEMPHYSCHEM Articles

Self-Assembled Graphene/MWCNT Bilayers as Platinum-Free Counter Electrode in Dye-Sensitized Solar Cells**

Ruri Agung Wahyuono,[a, b] Guobin Jia,[a] Jonathan Plentz,[a] Andrea Dellith,[a] Jan Dellith,[a] Felix Herrmann-Westendorf,[a, b] Martin Seyring,[c] Martin Presselt,[a, b] Gudrun Andrä,[a] Markus Rettenmayr,[c] and Benjamin Dietzek*[a, b, d]

We describe the preparation and properties of bilayers of graphene- and multi-walled carbon nanotubes (MWCNTs) as an alternative to conventionally used platinum-based counter electrode for dye-sensitized solar cells (DSSC). The counter electrodes were prepared by a simple and easy-to-implement double self-assembly process. The preparation allows for controlling the surface roughness of electrode in a layer-by-layer deposition. Annealing under N_2 atmosphere improves the electrode's conductivity and the catalytic activity of graphene and MWCNTs to reduce the I_3^- species within the electrolyte of the DSSC. The performance of different counter-electrodes is compared for ZnO photoanode-based DSSCs. Bilayer electrodes show higher power conversion efficiencies than monolayer graphene electrodes or monolayer MWCNTs electrodes. The bilayer graphene (bottom)/MWCNTs (top) counter electrode-based DSSC exhibits a maximum power conversion efficiency of 4.1% exceeding the efficiency of a reference DSSC with a thin film platinum counter electrode (efficiency of 3.4%). In addition, the double self-assembled counter electrodes are mechanically stable, which enables their recycling for DSSCs fabrication without significant loss of the solar cell performance.

1. Introduction

Dye-sensitized solar cells (DSSC) are third generation solar cells and have been intensively studied since their seminal report by O'Regan and Grätzel.[1] The most commonly used DSSC architecture consists of a dye-sensitized TiO_2 or ZnO photoanode and a counter electrode sandwiching a liquid electrolyte containing an iodine/triiodide redox couple.[1,2] The power conversion efficiency (PCE) of DSSCs has reached more than 13% and the production of DSSC modules has been demonstrated.[1–5]

Optimization of each of the individual components of a DSSC has been reported in literature, *i.e.* semiconductor photoanodes, molecular photosensitzers, electrolytes for redox mediation, and counter electrodes.[2–4] Among these components, the counter electrode plays a dual role:[3,4,6–11] It functions as a current collector but also catalyses the reduction of tri-iodide (I_3^-) to iodide (I^-), which is critical to regenerate the molecular sensitizers after electron injection and to ensure the continuous flow of charge through the solar cell. An optimized solar cell requires a counter electrode with low sheet resistance, high catalytic activity for the reduction of I_3^-, high chemical stability and low cost.[6–11] So far, thin film platinum is the standard for DSSC counter electrodes due to its high catalytic activity, conductivity and superior corrosion resistance against iodine species.[3,4,6] However, platinum as a relatively rare noble metal is expensive. Hence, it is appealing to exploit noble metal-free materials substituting the Pt counter electrode in DSSCs. Recent studies deal with this issue by focussing on, e.g., carbon nanomaterials, conductive polymers, and transition metal compounds.[6–9]

Among these materials for DSSC counter electrodes carbon nanomaterials such as carbon nanotubes (CNTs), graphene monolayer, 3D graphene nanostructures, *e.g.* honeycomb and cauliflower structure, and graphene flakes prepared from graphite present interesting options due to their low cost fabrication, controllable surface properties, high conductivity and catalytic activity.[12–20] Counter electrodes of activated carbon, single-walled carbon nanotubes (SWCNTs), and multi-walled carbon nanotubes (MWCNTs) in TiO_2-based DSSCs yield comparable efficiencies than Pt-counter electrodes.[3,4,6] However, the lower catalytic activity of these materials compared to Pt requires a large amount of carbon material to reach significant efficiencies. Consequently, the solar cell loses transparency – one of the

[a] R. A. Wahyuono, Dr. G. Jia, Dr. J. Plentz, A. Dellith, J. Dellith, F. Herrmann-Westendorf, Dr. M. Presselt, Dr. G. Andrä, Prof. Dr. B. Dietzek
Department Functional Interfaces
Leibniz Institute of Photonic Technology (IPHT)
Albert-Einstein-Str. 9, 07745 Jena, Germany
E-mail: benjamin.dietzek@leibniz-ipht.de
[b] R. A. Wahyuono, F. Herrmann-Westendorf, Dr. M. Presselt, Prof. Dr. B. Dietzek
Institute of Physical Chemistry and Abbe Center of Photonics, Friedrich Schiller University Jena
Helmholtzweg 4, 07743 Jena, Germany
[c] Dr. M. Seyring, Prof. Dr. M. Rettenmayr
Otto Schott Institute of Materials Research, Friedrich Schiller University Jena
Löbdegraben 32, 07743 Jena, Germany
[d] Prof. Dr. B. Dietzek
Center for Energy and Environmental Chemistry (CEEC), Friedrich Schiller University Jena
Philosophenweg 7a, 07743 Jena, Germany

[**] MWCNT: Multi-walled Carbon Nanotube

Supporting information for this article is available on the WWW under https://doi.org/10.1002/cphc.201900714

most striking features of DSSC with respect to applications e.g. in architecture. Graphene with its high carrier mobility (> 200 000 $cm^2 V^{-1} s^{-1}$ at an electron density of 4×10^9 cm^{-2}), high specific surface area (> 2300 $m^2 g^{-1}$), and semi-transparency in the visible range[15–20] has been used to fabricate counter electrodes. In particular when combined with SWCNTs and MWCNTs such carbon-based counter electrodes perform comparable to Pt- electrodes.[20–23] Various deposition technologies, e.g. spray coating, electrophoresis, inkjet printing and screen printing, have been applied to fabricate high-performance carbon-based electrodes.[24–27]

Previously we have developed a double self-assembly (DSA) process to deposit single layers of graphene on three-dimensional substrates.[28–30] This technique exploits surface interactions between graphene flakes and surfactant molecules at the water/air interface to deposit monolayer and multilayer structures of graphene on 3D substrate.[28,29] Compared to conventionally used deposition techniques (*vide supra*), DSA enables rapid deposition of graphene flakes on large areas even on hydrophobic 3D substrates. Additionally, DSA allows to deposit different 2D nanomaterials in a layer-by-layer sequence.[28–30] Here, DSA is used to prepare monolayer graphene and MWCNTs counter electrodes as well as bilayer graphene/MWCNTs electrodes on transparent conductive glass substrates. The DSA-processed carbon-electrodes are integrated into ZnO photoanode-based DSSCs and their performance, mechanical stability and recyclability are assessed. Instead of the widely used TiO_2 photoanode, ZnO photoanodes are employed due to its high electrochemical stability, slightly higher conduction band edge than TiO_2, and high electron mobility of ~150 $cm^2 V^{-1} s^{-1}$, which allow for the generation of a higher photovoltage and a rapid charge collection. In addition, the functional ZnO photoanodes[31,32] can be prepared at temperatures as low as 150 °C,[32] which is crucial when considering deposition of DSSCs on delicate substrates as *e.g.* textile fabrics. The results presented show the first approach towards nobel-metal free counter electrodes integrated into low-temperature processed ZnO-based DSSCs.

2. Results and Discussion

2.1. Optical, Structural, and Physical Properties

Conventional graphene- and MWCNTs-based counter electrodes require a large amount of carbon to yield efficiencies comparable to Pt-based counter electrodes.[3,4,6] This constraint causes carbon-based electrodes to become opaque preventing the DSSC to be used in back illumination or bifacial geometries. To test the optical properties of the DSA-deposited mono- and bilayer electrodes fabricated from graphene (G), MWCNTs, graphene (bottom) and MWCNTs (top) (G | MWCNTs), as well as MWCNTs (bottom) and graphene(top) (MWCNTs | G), transmission spectra are recorded (see Figure 1b). Although not highly transparent, the studied bilayer graphene- and MWCNTs-electrodes exhibit transmission up to 25% transmission in the visible wavelength range (vs. 80% transmission of the FTO glass substrate). The monolayer graphene electrode shows up to 60% transmission in the visible spectral range. The semi-transparent DSA-processed electrodes thus are suitable to be used in bifacial illumination and keep the solar cell (at least partially) transparent. N_2-annealing is found to alter the optical properties of graphene- and MWCNTs-based counter electrodes only marginally.

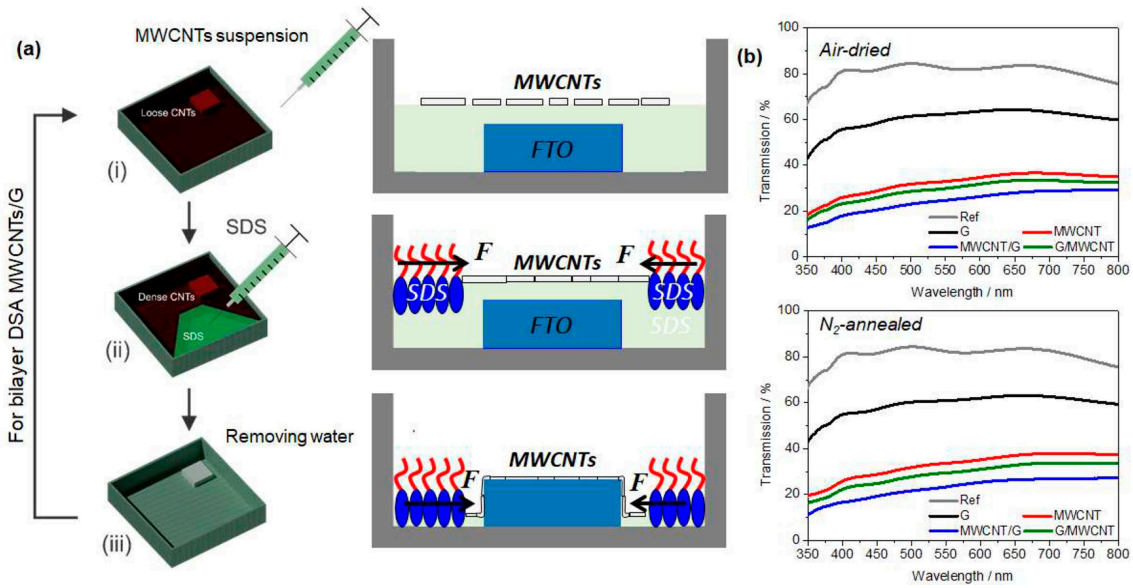

Figure 1. (a) Schematic overview of the double self-assembly process for the preparation of bilayer MWCNTs/graphene counter electrodes: (i) Injection of either loose MWCNTs or graphene suspension on the water surface of a petri dish with a transparent conductive (FTO) glass substrate inside, (ii) injection of SDS solution to increase the surface density of either MWCNTs or graphene flakes, and (iii) removing water. (b) The optical properties of different counter electrodes graphene/MWCNTs prepared by DSA process (*top*) before and (*bottom*) after annealing in N_2 atmosphere. As reference, the transmission spectrum of the FTO coated glass is presented.

The microstructural properties of the DSA-deposited graphene and MWCNTs monolayers are investigated by TEM and HRTEM (Figure 2). The structural quality of graphene and MWCNTs is evaluated by the position and the shape (azimuthal and radial width) of the reflections in the corresponding Fourier diffractograms. The azimuthal width reflects the undulation of the graphene layers, whilst the size of the coherent volume is calculated from the radial width. The mesh width of graphene and the intra-layer spacing in the MWCNTs, respectively, are quantified from the reflection positions[34] and summarized in Table S1 and Table S2 (in the Supporting Information). TEM images of the graphene flakes indicate wrinkled surfaces (Figure 2a) which are notably flattened (Figure 2b) upon annealing under N_2 due to thermal relaxation.[37] The flatter surface in annealed graphene layer manifests itself also in lower undulation angles than in air-dried graphene as shown by sharper reflections in the fast Fourier transform (FFT) image (inset Figure 2d). This lower undulation angles suggests a higher structural quality of the annealed graphene layer. Furthermore, annealing the graphene layer results in a slightly smaller mesh (d_{100}) compared to the pristine graphene, *i.e.* 2.12 *vs.* 2.09 Å, indicating shorter C–C bond lengths.

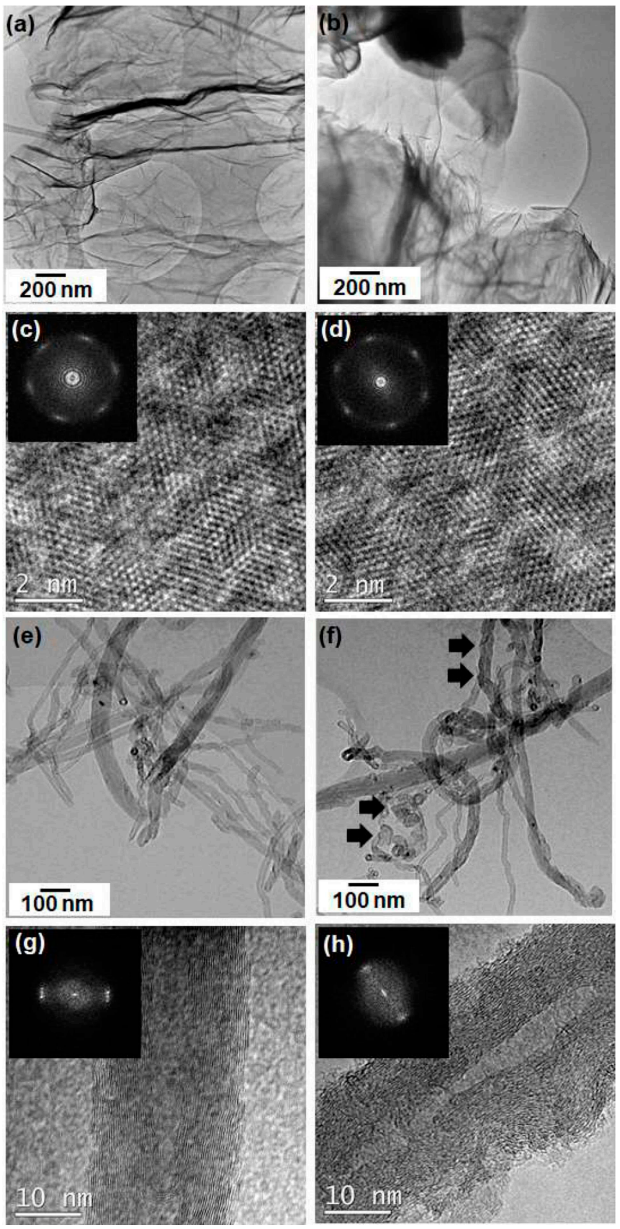

Figure 2. TEM and HRTEM images of monolayer graphene flakes (a,c) before and (b,d) after annealing, and MWCNTs (e,f) before and (g,h) after annealing. Inset of HRTEM images indicate the fast Fourier transform image to assess structural quality of graphene and MWCNTs.

To corroborate the above TEM/HRTEM analyses particularly on MWCNTs, Raman spectra are recorded for both air-dried and annealed samples (Figure S2 in the Supporting Information). The spectra of both samples show the D-band (~1467 cm^{-1}) which arises from defect-induced, double-resonant Raman scattering and the graphite-associated G-band (~1580 cm^{-1}) which corresponds to in-plane vibrations of sp^2-hybridized carbon atoms. The annealed MWCNTs display a higher D- to G-band intensity ratio (I_D/I_G), *i.e.* 0.97 *vs.* 0.85, than the air-dried samples. This higher I_D/I_G ratio reflects the fact that a notable fraction of defects is present in the annealed MWCNT samples.[38] Such defects, however, are known to be key for the high catalytic activity of carbon nanomaterials, which often stems from defect sites and atomic edges of graphene and MWCNTs.[6,7,11,15,17,19]

Annealing also induces surface imperfection in the MWCNTs, e.g. wavy outer surfaces of nanotube as denoted by short arrows in Figure 2f. Such imperfections, which possibly result from concentrated stress present during the annealing process,[36,37] are not observed in the air-dried samples. Even though the annealing temperature is far below the graphitization temperature (ca. 1800 °C), the HRTEM images show aligned graphene layers in air-dried MWCNTs while more defected graphene layers are observed upon annealing: The reflections for the annealed MWCNTs (FFT in Figure 2h) appear to be more diffuse indicating a lower structural quality. The reduced structural quality of annealed MWCNTs is reflected in a stronger undulation of the layers. The layer spacing in the annealed MWCNTs (d_{002} = 3.65 Å) is higher than for graphite (d_{002} = 3.355 Å) according to the curvature of the layers resulting in a non-perfect stacking.

Aside from the density and nature of the structural defects also the total surface area impacts the catalytic properties and hence the performance of carbon-based electrodes in electrochemical applications.[3,4] Figure 3a and Figure 3b depict the scanning electron micrographs of surface micromorphology of G|MWCNTs and MWCNTs|G, respectively. For the bilayer G|MWCNTs, the MWCNTs form a random porous network on top of the graphene flakes. The bilayer MWCNTs|G resembles a network of random nanotubes, 84% of which are covered (surface area coverage) by the graphene monolayer. Both structures thus reveal a graphene-MWCNT interface, which should principally be accessible and capable of I_3^--reduction upon integration of the carbon layers into DSSCs.

For Pt counter electrodes it is established that surface roughness impacts the (interfacial) charge transport.[39] Hence, rapid regeneration of redox shuttles in DSSCs can be achieved

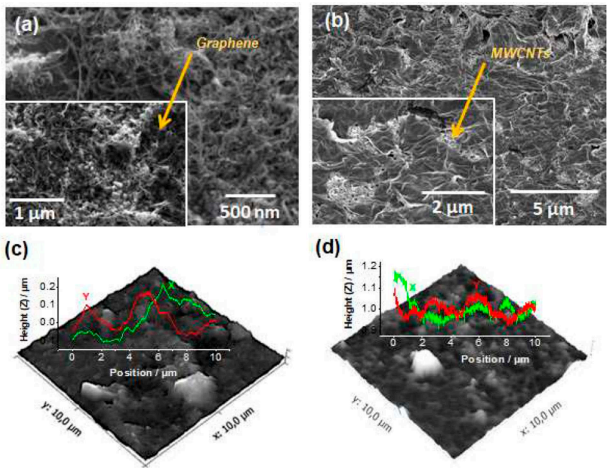

Figure 3. SEM images of the bilayer (a) G | MWCNTs and (b) MWCNTs | G counter electrode on fluorine-doped tin oxide substrate. AFM images of bilayer (c) MWCNTs | G, and (d) G | MWCNTs with the topographical height.

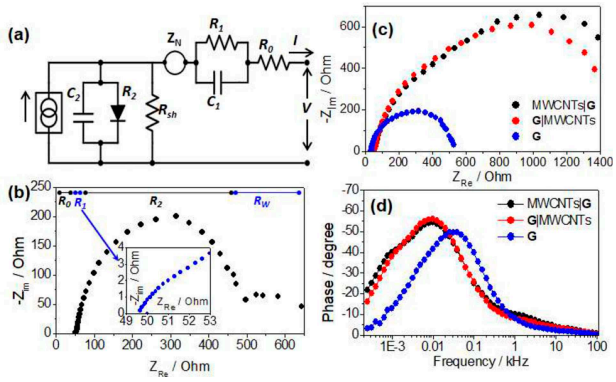

Figure 4. (a) A combined equivalent circuit model of DSSCs for EIS analysis adopted from literature. (b) Typical assignment of resistance (real part of impedance, Z_{Re}) derived from electrochemical impedance spectrum of DSSC utilizing MWCNTs-based counter electrodes. The Cole-cole plots are represented by (c) Nyquist plot and (d) Bode phase plot of DSSCs employing different N_2-annealed counter electrodes.

by surface modification.[39–41] The roughness of the DSA-fabricated electrodes is assessed by AFM measurements (Figure 3c–Figure 3d). In order to correlate surface roughness and catalytic activity of graphene- and MWCNTs-based counter electrodes, a roughness factor (RF) is defined as the ratio of the total surface area to the projected area of the counter electrodes.[40–42] The total surface area is measured by AFM, while the projected area is determined by optical microscopy. The calculated RFs for G, MWCNTs, G | MWCNTs, and MWCNTs | G are 2.41, 1.02, 1.04, and 1.71, respectively, indicating that the high surface roughness of the graphene DSA-monolayer shows contributes to the comparably high RF of bilayer MWCNTs | G.

2.2. Electrochemical Properties

To illustrate the factors underlying the performance of the counter electrodes, electrochemical impedance analysis of fully assembled DSSCs is carried out. The equivalent circuit models to fit the electrochemical impedance data are shown in Figure 4a. In this study, the capacitor (*C*) in the equivalent circuit model is replaced by the constant phase element (CPE) to compensate the non-ideal capacitive behaviour observed. The fitting results obtained *via* impedance analysis of DSSCs using different counter electrodes are summarized in Table 1. The Nyquist plot of DSSC (Figure 3b and Figure 4c) comprises three semicircles:[32,33] (i) the first small semicircle at high-frequencies (1–100 kHz) reflects the charge transfer process at the counter electrode/electrolyte interface (R_1); (ii) the large semicircle in the range 1 Hz–1 kHz is due to charge transfer at

Table 1. Electrochemical properties of different graphene and MWCNTs counter electrodes before and after N_2-annealing (indexed by _a) determined from impedance spectroscopy.

Counter Electrodes	R_1 [Ohm]	τ_1[a] (k_1) [ms (ms^{-1})]	j_0 [mA cm^{-2}]	D[b] [10^{-6} cm^2 s^{-1}]	R_2 [Ohm]	τ_2[a] (k_2) [ms (ms^{-1})]
G	41.3	21 (0.048)	2.634	0.52	327	41 (0.024)
G_a	6.3	4 (0.250)	17.268	1.09	250	34 (0.029)
MWCNTs	156.2	45 (0.022)	0.696	0.61	1315	515 (0.002)
MWCNTs_a	14.2	25 (0.040)	7.662	7.62	222	34 (0.029)
MWCNTs | G	71.4	33 (0.030)	1.523	1.58	656	149 (0.006)
MWCNTs | G_a	9.73	12 (0.083)	11.181	4.42	204	39 (0.026)
G | MWCNTs	215.9	91 (0.011)	0.503	0.31	914	195 (0.005)
G | MWCNTs_a	18.15	9 (0.111)	5.994	1.17	115	29 (0.034)

[a] $\tau = (R \times Q)^{1/\alpha}$ where R is the charge transfer resistance, *Q* is the admittance (CPE-P), and α is the non-ideality factor (CPE-T), where $0 < \alpha < 1$. [b] The diffusion coefficient is determined from the relation $\tau = B^2 = \delta^2/D$, where δ is the diffusion layer thickness ~15 µm.

the ZnO/dye/electrolyte interface (R_2); and (iii) the third small semicircle at low frequencies (<1 Hz) is assigned to the charge transport in the electrolyte. A qualitative view of the Nyquist plots for different electrodes shows remarkably different sized semicircles, indicating very different charge transfer characteristics from different counter electrodes.

We focus on the impedance at high frequencies, which is associated with the charge transfer at the interfaces of counter electrode/electrolyte. The associated parameters R_1 and τ_1 denote the corresponding charge transfer resistance and the time constant for I_3^- reduction, respectively. Annealing reduces R_1 significantly (for the graphene layers from 41.3 to 6.3 Ω and for MWCNT electrodes from 156.2 to 14.2 Ω). This contributes to faster charge transfer kinetics at the counter electrode for I_3^- reduction (k_1 is increased from 0.048 to 0.250 ms^{-1} for graphene and from 0.022 to 0.040 ms^{-1} for the MWCNT electrode) and diffusion of I_3^- in the liquid electrolyte. Since I_3^- is the current limiting species in the electrolyte,[42,43] diffusion affects the dye regeneration kinetics and hence, higher diffusion coefficient *D* facilitates higher device performance. For annealed bilayer electrodes, the peak shifts to lower frequencies found in the Bode phase plot suggest altered charge transfer kinetics compared to DSSC with monolayer graphene electrodes. This frequency shift is corroborated by the fitting results which show a slower rate of I_3^- reduction at counter electrode/electrolyte interface for bilayer MWCNTs|G (k_1 = 0.083 ms^{-1}) and G|MWCNTs (k_1 = 0.111 ms^{-1}) than for MWCNTs (k_1 = 0.040 ms^{-1}).

Han and co-workers reported that R_1 is inversely proportional to the RF for sputtered Pt countered electrodes. Also for the DSA-carbon electrodes prepared here, such linear relationship between R_1 and 1/RF is observed (Figure 5a). This suggests that an increase of surface roughness accelerates I_3^- reduction. It should be noted that lower R_1 values are required to obtain high solar cell performances as the exchange current density (j_0) at the counter electrode relates to R_1 as $j_0 = \frac{RT}{nFR_1}$.[11] *R* denotes the universal gas constant, *T* is the absolute temperature, *F* is the Faraday constant, *n* is the stoichiometric number of electrons involved in a reaction. Practically, j_0 higher than the photocurrent density generated at the photoanode is desirable. For each of the counter electrodes Table 1 summarizes the exchange current densities obtained. N_2-annealing significantly improves j_0 indicating enhanced catalytic activity for the reduction of I_3^-. The enhanced catalytic activity is caused by higher density of catalytically active sites, which are available due to structural defects formed upon annealing as revealed by TEM and Raman study (*vide supra*). The trend of the exchange current density recorded at different graphene and MWCNTs electrodes is corroborated by the cyclic voltammogram shown in Figure 5b. The graphene-based electrode exhibits the highest current density (8 mA cm^{-2}) while the G|MWCNTs-based electrode yields only 3.6 mA cm^{-2}. As the exchange current density at an electrode interface is inversely proportional to its charge transfer resistance, all counter electrodes investigated here exhibit higher exchange current densities than the ZnO photoanode. This can be seen from R_1 being one order of magnitude smaller than R_2 (see Table 1), *i.e.* the charge transfer resistance at photoanode ZnO/dye/electrolyte interfaces.

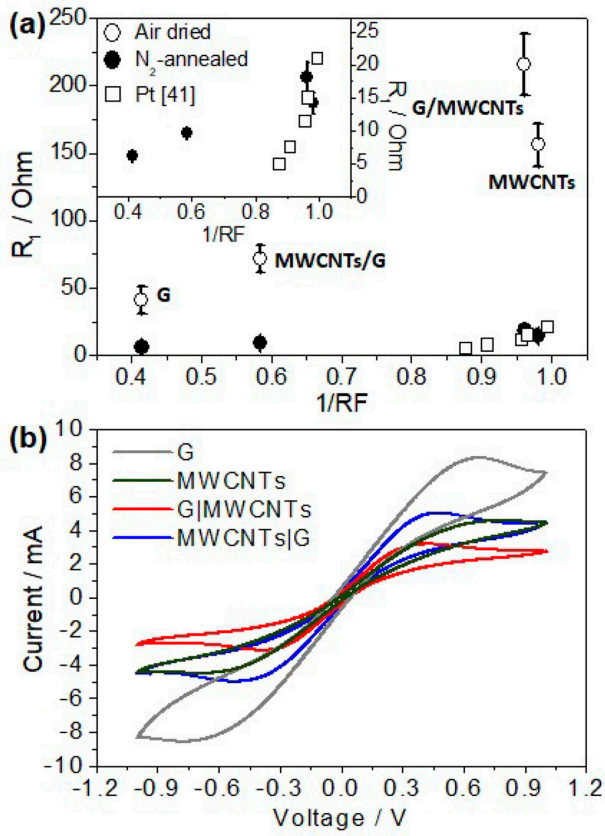

Figure 5. (a) A combined equivalent circuit model of DSSCs for EIS analysis adopted from literature. (b) Typical assignment of resistance (real part of impedance, Z_{Re}) derived from electrochemical impedance spectrum of DSSC utilizing MWCNTs-based counter electrodes. The Cole-cole plots are represented by (c) Nyquist plot and (d) Bode phase plot of DSSCs employing different N_2-annealed counter electrodes.

2.3. Solar-Cell Performance

DSSCs were fabricated to evaluate the power conversion efficiencies of the solar cells with both double self-assembled graphene- and MWCNTs-based counter electrodes. The architecture of the sandwiched DSSCs architecture is shown in Figure 6(a). The current density-voltage (*J-V*) curves of graphene- and MWCNTs-based DSSCs recorded under 1000 W m^{-2} AM1.5 irradiation are given in Figure 6(b). The *J-V* curve of thin film Pt counter electrode based DSSC is also shown for reference. The solar cell parameters, including open-circuit (V_{oc}), short-circuit photocurrent density (J_{sc}), fill factor (FF), and power conversion efficiency (η) are summarized in Table 2. Compared to the reference Pt-based solar cell, the DSSC with G/MWCNTs counter electrodes show improved performance parameters of V_{oc} = 0.62 V, J_{sc} = 13.3 mA cm^{-2}, a fill factor (FF) = 0.49, and an efficiency (η) = 4.1 %.

The improved performance of the solar cells with carbon-based DSA-electrodes is related to the catalytic activity of the counter electrode. Annealing of the counter electrode enhances both J_{sc} and the FF, while the effect on V_{oc} is minor. The increase of J_{sc} is related to an enhanced catalytic activity for the

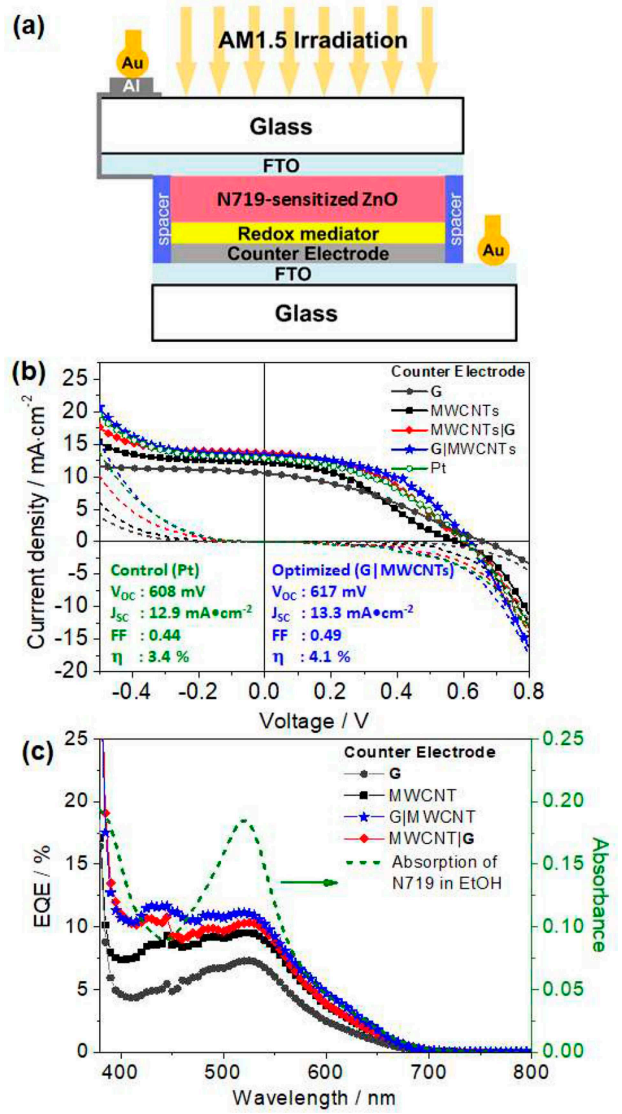

Figure 6. (a) Sandwich structure of ZnO-based DSSC using different counter electrodes, (b) *J-V* of ZnO-based DSSCs using different counter electrodes measured under 100 mW cm^{-2} AM1.5 irradiation (solid line) and in the dark (dashed line). (c) EQE curves of ZnO-based DSSCs using different counter electrodes. The counter electrodes used in the DSSC were annealed under N_2 atmosphere.

Table 2. Solar cell properties of different double self-assembled graphene- and MWCNTs-based counter electrodes before and after N_2-annealing (indexed by _a). The best recorded ZnO-based solar cell using Pt counter electrodes is 7.4% (V_{oc} = 0.640 V, J_{sc} = 19.8 mA cm^{-2}, FF = 0.59).[44]

Counter Electrode	V_{oc} [V]	J_{sc} [mA cm^{-2}]	FF	H [%]
G	0.702	9.8	0.21	1.5
G_a	0.676	10.9	0.29	2.1
MWCNTs	0.542	12.1	0.24	1.6
MWCNTs_a	0.568	12.4	0.33	2.4
MWCNTs|G	0.566	12.6	0.27	1.9
MWCNTs|G_a	0.604	13.7	0.43	3.6
G|MWCNTs	0.564	12.1	0.28	1.9
G|MWCNTs_a	0.617	13.3	0.49	4.1
Pt	0.608	12.9	0.43	3.4

reduction of I_3^-. The FF is affected by total series resistance (R_s)[9,39–41] which is the sum of sheet resistance (R_0), charge transfer resistance at counter electrode interface (R_1) and bulk electrolyte resistance: $FF = FF_0(1\text{-}r_s)$. Here, FF_0 denotes the fill factor not affected by series resistance, and $r_s = R_s/R_{ch} = (I_{sc} \times R_s)/V_{oc}$.[37,38]

The overall solar cell performance is assessed by *J-V* curves measured under 100 mW cm^{-2} AM1.5 irradiation (Figure 5b). The lowest conversion efficiency is obtained using a monolayer graphene electrode. Despite moderate conversion efficiency, the DSSCs using a monolayer MWCNTs counter electrode exhibit low FF as there is S-shape of J–V curves around open circuit voltage (see Figure 6). This S-shape might be due to back charge transfer at the counter electrode, as the conductive substrate is not completely covered by MWCNTs, and a higher Schottky barrier at the TCO/MWCNTs interface.[45,46] Figure 6c presents external quantum efficiency (EQE) spectra: a broad EQE spectrum from 400 to 600 nm peaking at 520 nm characterizes the spectral response of the photocurrent generated in each DSSC. The EQE spectra with yields ranging from 2–15% resemble the absorption feature of N719[2] (for chemical structure see Supporting Information), which is used as photosensitizer. To corroborate the different net photocurrent generated in DSSC using different counter electrodes the individual EQE spectrum is integrated, as J_{sc} in DSSCs shall scale with the integrated EQE spectra over the wavelength range of irradiation.[2] The results are consistent with the photocurrent density determined from the *J-V* curves: Using MWCNTs|G as counter electrode yields higher photocurrents, by factor of 1.8 (EQE spectrum) and 1.4 (*J-V* curve), than an annealed monolayer graphene counter electrode.

Amongst the N_2-annealed samples, the bilayer MWCNTs|G and G|MWCNTs counter electrodes yield higher power conversion efficiencies compared to the reference solar cell, *i.e.*, 6 and 21% higher than Pt counter electrode-based DSSC (η = 3.4%) for MWCNTs|G (η = 3.6%) and G|MWCNTs (η = 4.1%), respectively. For monolayer structures, the utilization of MWCNTs-based counter electrodes results in efficiencies of 3.2% comparable to the Pt counter electrode, while monolayer graphene counter electrode exhibits lower efficiency (η ~2.1%). Compared to literature reports on related systems, *i.e.* ZnO-DSSCs with carbon-based counter electrodes, the DSA-electrodes introduced here perform at least at par. The best efficiency obtained in this study (η = 4.1% using the bilayer G|MWCNT electrode) exceeds the efficiencies reported by Pandikumar and coworkers,[47] who report efficiencies of 2% using a polypyrrole/rGO/p-toluenesulfate composite as counter electrode. The solar cells reported here also outperform solar cells, in which the ZnO anode is sensitized by quantum dots and an ordered mesocellular carbon foam functions as counter electrode. This concept yields a maximum efficiency of 3.6% (V_{oc} = 0.685 V, J_{sc} = 12.6 mA cm^{-2}, and FF = 0.42).[48] Kilic and Turkdogan report a ZnO photoanode in combination with a FeS_2/graphene counter electrode, with a superior efficiency of 5.1%.[49] Further optimization of graphene or MWCNTs counter electrode performance might include Na and MoS_2 modification as well as chemical oxidation on the N_2-annealed graphene or MWCNTs

surface.[8,50] Park and co-workers reported that chemical oxidation of MWCNTs using sulfuric acid/nitric acid (H_2OS_4/HNO_3) or potassium persulfate/sodium hydroxide ($K_2S_2O_8$/NaOH) also yields conductivity up to ten folds higher than pristine MWCNTs and boosts the solar cell efficiency from 0.2 to 1.3 %.[50b] Hu and co-workers reported that embedding Na on the carbon counter electrode doubles the conductivity and hence, increases FF up to 0.66 when used with TiO2-based photoanodes.[50c]

The DSSCs using graphene or MWCNTs counter electrode exhibit lower FF compared to the current record ZnO-based solar cells using Pt counter electrodes.[44] However, the record efficiency is achieved for 450 °C annealed ZnO photoanode in the presence of a blocking layer. At the lower annealing temperature processed ZnO photoanode and without blocking layer, the best reported conversion efficiency is only 2.6 % (V_{oc} = 0.650 V, J_{sc} = 7.5 mA cm^{-2}, and FF = 0.54).[46] The highest V_{oc} and J_{sc} value obtained in this study is 0.676 mV and 13.7 mA/cm^2, respectively. Considering that the performance of graphene or MWCNTs counter electrode can be further optimized using chemical oxidation, these solar cell parameters imply that low temperature processed ZnO-based solar cell using double self-assembled graphene/MWCNTs counter electrode are indeed promising dye-sensitized solar cell architecture.

2.4. Physical Stability and Recyclability of Bilayer MWCNTs | G

Re-using counter electrodes in DSSCs is useful and cost-efficient: various parameters (e.g. differently sensitized anodes) could be evaluated with *one* counter electrode. For such an approach to work, the counter electrode has to be chemically and mechanically stable and has to produce highly reproducible results. In this context, the stability of the DSA-bilayer MWCNTs | G during recycling is assessed. Each cycle involves washing using acetonitrile to remove the physisorbed electrolytes (we compare Li^+-containing and Li^+-free iodine-based electrolytes) and addition of fresh electrolyte for the new solar cell assembly. Figure 7 shows SEM images of a MWCNTs | G surface after being recycled five times. The dark area is the graphene monolayer, while the bright areas show the MWCNTs in the bottom layer. As seen in Figure 7a, the surface of MWCNTs | G is covered with large particles after being used in DSSCs with the Li^+-containing electrolyte. The EDX spectra recorded at the MWCNTs | G sites covered with the particles (Figure 7d) show N and I peaks indicating the presence of intercalated alkylammoinum and Li^+-ions from the tertbutylammonium and lithium iodide, respectively. This is further confirmed by X-ray diffraction analysis (Figure S7 in the Supporting Information). Such intercalation of Li^+ and alkylammonuim ions has been shown to exfoliate carbon nanotubes creating a new layer of graphene, hence, modifying the surface properties of carbon nanotube-based electrodes.[51–54] In contrast, the surface of the MWCNTs | G electrolyte operated with the Li^+-free electrolyte remains uncontaminated.

To assess the stability of the graphene monolayer covering the MWCNTs, Raman spectra are collected before and after recycling (Figure 7b and Figure 7c). The G and 2D band

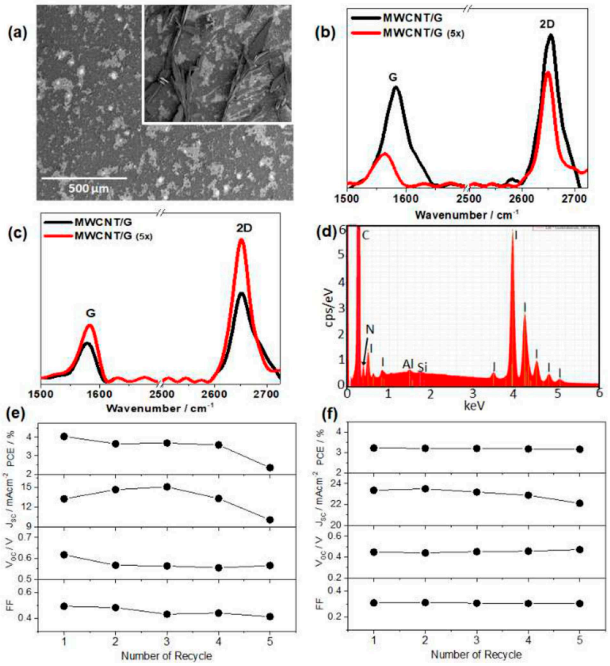

Figure 7. (a) Scanning electron micrograph of bilayer MWCNTs | G counter electrodes after recycled in DSSC employing (inset) Li^+- iodine based electrolyte and Li^+-free iodine based electrolyte consisting of alkylbenzimidazole, 1-ethyl-3-methylimidazolium iodide; 1,3-dimethylimidazolium iodide, 1-ethyl-3-methylimidazolium tetracyanoborate. Raman spectra of bilayer MWCNTs | G counter electrodes before (black spectra) and after (red spectra) usage in DSSC in contact with (a) Li^+-iodine based electrolyte and (b) Li^+-free iodine based electrolyte. (d) The EDX spectrum of bilayer MWCNTs | G counter electrodes after usage in DSSC in contact with Li^+-iodine based electrolyte. Solar cell properties of DSSCs using bilayer MWCNTs/graphene and (e) Li^+-iodine and (f) Li^+-free iodine based electrolyte at different state of counter electrode's recycle.

intensities at ~1580 and 2650 cm^{-1}, respectively, indicate the quality and number of graphene layers.[55] The ratio I_{2D}/I_G indicates the number of graphene layer; $I_{2D}/I_G = 2$ is characteristic for a graphene monolayer.[56,57] The I_{2D}/I_G ratio of the MWCNTs | G electrode operated with a Li^+-free electrolyte is not significantly altered upon recycling, *i.e.*, 2.2 (before) and 2.4 (after the fifth cycle). This indicates that the double self-assembled graphene monolayer adheres strongly to the MWCNTs yielding a robust surface integrity. Meanwhile, using a Li^+-containing electrolyte, I_{2D}/I_G increases significantly from 1.9 to 4 (Figure 7). This change suggests that more than one layer of graphene is built on top of the MWCNT layer likely due to exfoliation of MWCNTs upon intercalation of Li^+ and tertbutylammonium ions contained in electrolyte.

The performance of the recycled MWCNTs | G counter electrodes in DSSCs is shown in Figure 7e and Figure 7f. Despite a lower initial solar cell efficiency using Li^+ free electrolyte (η = 3.22 %, V_{oc} = 0.450 V, J_{sc} = 23.4 mA cm^{-2}, FF = 0.31), the counter electrodes enable fabrication of recyclable solar cells with efficiency of 3.14 %, (V_{oc} = 0.470, J_{sc} = 22.1 mA cm^{-2}, FF = 0.30). In contrast, the solar cell employing Li^+ containing electrolyte suffers from a significantly decrease of the power conversion efficiency from 4.0 % (V_{oc} = 0.617, J_{sc} = 13.3 mA cm^{-2}, FF = 0.49)

to 2.36% (V_{oc} = 0.566, J_{sc} = 10.7 mA cm^{-2}, FF = 0.41) after five recycling process. This PCE decrease is due to the exfoliation of MWCNTs reducing the catalytic activity of the counter electrode.

3. Conclusions

We have demonstrated an alternative straight forward, flexible and low cost fabrication procedure for Pt-free counter electrodes for dye-sensitized solar cells employing graphene and multi-walled carbon nanotubes (MWCNTs). The double self-assembly (DSA) process demonstrated here produces monolayer and bilayer graphene- and MWCNTs-based counter electrodes. Annealing under N_2 atmosphere enhances the catalytic activity of the counter electrodes to reduce tri-iodide in the electrolyte of the DSSCs. The surface roughness of graphene- and MWCNTs-based counter electrodes is a critical parameter to control since it impacts the charge transfer resistance, which in turn is associated with the catalytic efficiency of the counter electrodes. The rougher surface of graphene- and MWCNTs-based counter electrodes corresponds to an enlarged active surface area, which enhances the catalytic reduction of iodide species in electrolyte. The DSA processed graphene- and MWCNTs-based counter electrodes exhibit good mechanical stability. Their mechanical and chemical stability allows for recycling the all-carbon counter electrodes for re-fabrication of DSSCs without notable loss in efficiency.

Experimental Section

Preparation of the MWCNTs and Graphene Suspensions

50 mg MWCNTs (Ossila Ltd.) functionalized with –COOH group were suspended in 10 ml iso-propanol. The semi-stable suspension was homogenized via ultrasonication for 30 min shortly before deposition. Thermally reduced graphene oxide flakes[33] suspended in water (~5 g/l) were used as starting material for the graphene deposition. The suspension was dried in a furnace and subsequently re-suspended in ethanol at the same concentration.

Deposition of the Bilayer MWCNTs/MGFs by Double Self-Assembly (DSA)

Fluorine doped tin oxide (FTO) coated glass substrates were placed in a petri dish and cleaned by rinsing with acetone. After drying of the substrates and the petri dish under a N_2 stream, the dish was filled with deionized (DI) water until the FTO coated glasses were completely submerged. Using a syringe, about 0.5 ml of the MWCNTs suspension in ethanol was slowly dispersed on the water surface. The MWCNTs assemble to a uniform layer floating on the water surface. At the edge of the petri dish, approximately 0.1 ml of sodium dodecyl sulfate (SDS) solution (10 wt.% in water) was dropwise added to the water. The SDS molecules spread on the water surface, pushing the MWCNTs aside to form a dense layer. The MWCNTs layer is transferred onto the FTO by removing the water.[30] The samples were dried in a furnace at 80 °C for 15 min.

After drying, the samples coated with MWCNTs were placed in another clean petri dish, and DI-water was added until the samples were fully immersed. It was ensured that complete drying of the MWCNTs layers does not lead to detachment of the layers from the FTO. To form the bilayer, about 0.2 ml of the graphene suspension is added on the water surface using a syringe. The graphene flakes form a loose monolayer floating on the water surface. Approximately 0.1 ml of a SDS solution (10 wt.% in water) was added at the edge of the petri dish, compressing the graphene flakes to form a dense layer. This layer is subsequently deposited on top of the MWCNT layer by removal of the water. The samples are then again dried as described above. For the deposition of the MGFs/MWCNTs bilayer, the deposition sequence of the above-described process has simply to be inverted. Before assembly of functional DSSCs, the electrodes were annealed under N_2 atmosphere at 500°C for 30 min to further reduce the grapheme and MWCNTs and to improve the electrical properties. Schematic representation of each step in the DSA process is illustrated in Figure 1a.

Characterization of the Physical and Optical Properties of DSA-Processed Counter Electrodes

The morphology of the carbon-based electrodes is assessed using a FEI Helios NanoLab G3 UC. The secondary electron (SE) images were taken at 5 keV electron energy with a specimen tilt of 30°. Transmission electron microscopy (TEM) and high-resolution transmission electron microscopy (HRTEM) for graphene were carried out using a JEOL NEOARM 200F operating at 80 kV equipped with a cold field emission gun and 4k×4k Gatan OneView CCD-camera. TEM and HRTEM for MWCNTs were performed with a JEOL 3010HT operating at an acceleration voltage of 300 kV that equipped with a LaB6 emitter and a 1k×1k Gatan multi scan CCD-camera. Surface topography and roughness were characterized by atomic force microscopy (AFM) with a dimension edge system (Bruker). A silicon AFM probe was used in tapping (intermittent) mode within an active area of 5×5 and 10×10 μm^2, respectively. The optical transmission of the counter electrodes was measured using a Varian-Cary UV-vis-NIR spectrometer. Raman spectra of the carbon-based electrodes were collected upon excitation at 785 nm (Raman-HR-TEC, StellarNet).

Dye-Sensitized Solar Cell Fabrication and Electrochemical Characterization

Sandwiched DSSCs structures were fabricated according to our previous works:[32] ZnO paste was deposited on FTO substrate and heated at 150 °C for 2 h. The ZnO films used as photoanodes were sensitized by soaking in a 0.5 mM ethanolic solution of the Solaronix dye N719. DSA-processed carbon-based electrodes and thin film Pt electrodes were employed as counter electrodes. The photoanode and the counter electrode are assembled on top of each other using a film spacer (parafilm) of approximately 50 μm. A small amount of electrolyte containing 0.5 M tetrabutylammonium iodide, 0.1 M lithium iodide, 0.1 M iodine and 0.5 M 4-*tert*-butylpyridine in acetonitrile was injected into the inter-electrode space.

The photocurrent-voltage (J–V) curves are measured under 100 mWcm^{-2} irradiation (AM1.5, solar simulator). Electrochemical characterization was carried out using cyclic voltammetry and electrochemical impedance spectroscopy. Electrochemical measurements were performed with a computer-controlled potentiostat (Princeton Applied Research VersaSTAT MC potentiostat) equipped with a frequency response analyzer in the range between 0.1 Hz and 100 kHz. Impedance measurements were carried out both under illumination from a xenon lamp and in the dark. The spectra were fitted with the Z-View software (v3.2c, Scribner Associate, Inc.) in terms of appropriate equivalent circuits.[32]

EQE is determined with a home-built setup.[58,59] Light from a 1000 W Xe lamp attached to a 260 mm triple grating monochromator modulated by mechanical chopping at 83 Hz. The sample is irradiated on an area of 6.0×1.3 mm^2. Current measurements were performed using a 50 Ohm resistor as load and measuring the voltage drop over the load with a second SR830 Lock-In amplifier. To obtain absolute quantum efficiencies, a standard silicon solar cell was used as reference. The EQE of the standard cell was validated by a commercial setup from Bentham instruments.

Acknowledgements

The authors thank Barbara Geisenhainer and Christa Schmidt for the optical measurements and XRD measurement, respectively. Financial support by the Free State of Thuringia within the project "FEST" (2016 FE 9028) and co-funding by the European Union within the European Regional Development Fund (ERDF) are acknowledged. Furthermore, financial support by DFG (Inst 275/391-1) and the "Bundesministerium für Bildung und Forschung" (FKZ: 03EK3507) is highly acknowledged.

Conflict of Interest

The authors declare no conflict of interest.

Keywords: counter electrode · double self-assembly process · dye-sensitized solar cells · graphene flakes · MWCNTs

[1] B. O'Regan, M. Grätzel, *Nature* **1991**, *353*, 737–740.
[2] A. Hagfledt, G. Boschloo, L. Sun, L. Kloo, H. Pettersson, *Chem. Rev.* **2010**, *110*, 6595–6663.
[3] S. Yun, A. Hagfeldt, T. Ma, *Adv. Mater.* **2014**, *26*, 6210–6237.
[4] M. Wu, T. Ma, *J. Phys. Chem. C* **2014**, *118*, 16727–16742.
[5] M. A. Green, K. Emery, Y. Hishikawa, W. Warta, E. D. Dunlop, *Progress in Photovoltaics: Research and Applications* **2015**, *24*, 3–11.
[6] S. Thomas, T. G. Deepak, G. S. Anjusree, T. A. Arun, S. V. Nair, A. S. Nair, *J. Mater. Chem. A* **2014**, *2*, 4474–4490.
[7] J. Velten, A. J. Mozer, D. Li, D. Officer, G. Wallace, R. Baughman, A. Zakhidov, *Nanotechnology* **2012**, 23, 085201.
[8] a) Z. Zang, M. Liu, C. Zhang, W. W. Tjiu, T. Liu, H. Peng, *Angew. Chem. Int. Ed.* **2013**, *52*, 3996–3999; *Angew. Chem.* **2013**, *125*, 4088–4091; b) W. Wei, K. Sun, Y. H. Hu, *J. Mater. Chem. A* **2016**, *4*, 12398–12401.
[9] F. Herrmann, S. Engmann, M. Presselt, H. Hoppe, S. Shokhovets, G. Gobsch, *Appl. Phys. Lett.* **2012**, *100*, 153301.
[10] Y. Xue, J. Liu, H. Chen, R. Wang, D. Li, J. Qu, L. Dai, *Angew. Chem. Int. Ed.* **2012**, *51*, 12124–12127; *Angew. Chem.* **2012**, *124*, 12290–12293.
[11] T. Battumur, S. H. Mujawar, Q. T. Truong, S. B. Ambade, D. S. Lee, W. Le, S. H. Han, S. H. Lee, *Curr. Appl. Phys.* **2012**, 12, e49-e53.
[12] J. D. Roy-Mayhew, D. J. Bozym, C. Punckt, I. A. Aksay, *ACS Nano* **2010**, 4, 6203–6211.
[13] H. Choi, H. Kim, S. Hwang, W. Choi, M. Jeon, *Sol. Energy Mater. Sol. Cells* **2011**, *95*, 323–325.
[14] D. W. Zang, X. D. Li, H. B. Li, S. Chen, Z. Sun, X. J. Yin, S. M. Huang, *Carbon* **2011**, 49, 5382–5388.
[15] A. Kaniyoor, S. Ramaprabhu, *J. of Appl. Phys.* **2011**, *109*, 124308.
[16] L. Kavan, J. Yum, M. Gratzel, *ACS Nano* **2011**, *5*, 165–172.
[17] a) H. Wang, Y. H. Hu, *Energy Environ. Sci.* **2012**, *5*, 8182; b) H. Wang, K. Sun, F- Tao, D. J. Stacchiola, Y. H. Hu, *Angew. Chem. Int. Ed.* **2013**, *52*, 9210–9214; *Angew. Chem.* **2013**, *125*, 9380–9384; c) W. Wei, K. Sun, Y. H. Hu, *J. Mater. Chem. A*, **2013**, 2, 16842–16846.
[18] X. Huang, Z. Zeng, Z. Fan, J. Liu, H. Zhang, *Adv. Mater.* **2012**, *24*, 5979–6004.
[19] Z. Yin, J. Zhu, Q. He, X. Cao, C. Tan, H. Chen, Q. Yan, H. Zhang, *Adv. Energy Mater.* **2014**, *4*, 1300574.
[20] V. D. Dao, L. L. Larina, H. Suh, K. Hong, J. K. Lee, H. S. Choi, *Carbon* **2014**, *77*, 980–992.
[21] V. D. Dao, Y. Choi, K. Yong, L. L. Larina, H. S. Choi, *Carbon* **2015**, *84*, 383–389.
[22] H. Zhang, C. Yang, Z. Du, D. Pan, X. Zhong, *J. Mater. Chem. A* **2017**, *5*, 1614–1622.
[23] A. A. Memon, A. A. Arbab, I. A. Sahito, K. C. Sun, N. Mengal, S. H. Jeong, *Sol. Energy* **2017**, *150*, 521–531.
[24] S. Casaluci, M. Gemmi, V. Pellegrini, A. D. Carlo, F. Bonaccorso, *Nanoscale* **2016**, *8*, 5368–5378.
[25] D. Dodoo-Arhin, R. C. T. Howe, G. Hu, Y. Zhang, P. Hiralal, A. Bello, G. Amaratunga, T. Hasan, *Carbon* **2016**, *105*, 33–41.
[26] H. Choi, H. Kim, S. Hwang, Y. Han, M. Jeon, *J. Mater. Chem.* **2011**, *21*, 7548.
[27] G. Zhu, L. Pan, T. Lu, T. Xu, Z. Sun, *J. Mater. Chem.* **2011**, 21, 14869.
[28] G. Jia, J. Plentz, M. Presselt, J. Dellith, A. Dellith, S. Patze, J. Tölle, R. Mülhaupt, G. Andrä, F. Falk, B. Dietzek, *Adv. Matter. Interfaces* **2017**, *4*, 1700758.
[29] G. Jia, J. Plentz, J. Dellith, A. Dellith, R. A. Wahyuono, G. Andrä, *Coating* **2019**, *9*, 183.
[30] G. Jia, J. Westphalen, J. Drexler, J. Plentz, J. Dellith, A. Dellith, G. Andrä, F. Falk, *Photonics Nanostruct.* **2016**, *19*, 64–70.
[31] a) J. A. Anta, Elena Guillén, R. Tena-Zaera, *J. Phys. Chem. C* **2012**, *116*, 11413–11425; b) Q. Zhang, C. S. Dandeneau, X. Zhou, G. Cao, *Adv. Mater.* **2009**, *21*, 4087–4108; c) R. A. Wahyuono, D. D. Risanti, T. Shirosaki, S. Nagaoka, M. Takafuji, H. Ihara, *AIP Conf. Proc.* **2014**, *1586*, 78–81; d) Ü. Özgür, Y. I. Alivov, C. Liu, A. Teke, M. A. Reshchikov, S. Dogan, V. Avrutin, S.-J- Cho, H. Morkoc, *J. Appl. Phys.* **2005**, *98*, 1–103.
[32] a) R. A. Wahyuono, F. Hermann-Westendorf, A. Dellith, C. Schmidt, J. Dellith, J. Plentz, J. Schulz, M. Presselt, M. Seyring, M. Rettenmeyer, B. Dietzek, *Chem. Phys.* **2017**, 483–484, 112–121; b) R. A. Wahyuono, B. Schulze, M. Rusu, M. Wächtler, J. Dellith, M. Seyring, M. Rettenmayr, J. Plentz, A. Ignaszak, U. S. Schubert, B. Dietzek, *ChemPlusChem* **2016**, *81*, 1281–1291.
[33] F. J. Tölle, M. Fabritius, R. Mülhaupt, *Adv. Funct. Mater.* **2012**, *22*, 1136–1144.
[34] M. Seyring, A. Simon, I. Voigt, U. Ritter, M. Rettenmayr, *Carbon* **2017**, *116*, 347–355.
[35] Y.-C. Lin, C.-C. Lu, C.-H. Yeh, C. Jin, K. Suenaga, P.-W. Chiu, *Nano Lett.* **2012**, *12*, 414–419.
[36] Y. A. Kim, H. Muramatsu, T. Hayashi, M. Endo, M. Terrones, M. S. Dresselhaus, *Chem. Phys. Lett.* **2004**, *398*, 87–92.
[37] Y. A. Kim, T. Hayashi, K. Osawa, M. S. Dresselhaus, M. Endo, *Chem. Phys. Lett.* **2003**, *380*, 319–324.
[38] H. Behler, S. Osswald, H. Ye, S. Dimovski, Y. Gogotsi, *J. Nano. Res.* **2006**, *8*, 615–625.
[39] N. Koide, A. Islam, Y. Chiba, L. Han, *J. Photochem. Photobiol. A* **2006**, *182*, 296–305.
[40] L. Han, N. Koide, Y. Chiba, A. Islam, T. Mitate, *C. R. Chim.* **2006**, *9*, 645–651.
[41] L. Han, N. Koide, Y. Chiba, T. Mitate, *Appl. Phys. Lett.* **2004**, *84*, 2433–2435.
[42] P. Wyss, T. Moehl, S. M. Zakeeruddin, M. Grätzel, *J. Mater. Chem.* **2012**, *22*, 24424.
[43] A. Hauch, A. Georg, *Electrochim. Acta* **2001**, *46*, 3457–3466.
[44] N. Memarian, I. Concina, A. Braga, S. M. Rozati, A. Vomiero, G. Sberveglieri, *Angew. Chem. Int. Ed.* **2011**, *50*, 12321–12325; *Angew. Chem.* **2011**, *123*, 12529–12533.
[45] L. Zuo, J. Yao, H. Li, H. Chen, *Sol. Energy Mater. Sol. Cells* **2014**, *122*, 88–93.
[46] B. Romero, G. del Pozo, B. Arrendondo, D. Martín-Martín, M. P. R. Gordoa, A. Pickering, A. Pérez-Rodríguez, E. Barrena, F. J. García-Sánchez, *IEEE Trans. Electron Devices* **2017**, *64*, 4622–4627.
[47] F. A. Jumeri, H. N. Lim, Z. Zainal, N. M. Huang, A. Pandikumar, S. P. Lim, *J. Power Sources* **2015**, *293*, 712–720.
[48] M. Seol, M. Ramasamy, J. Lee, K. Yong, *J. Phys. Chem. C* **2011**, *115*, 22018–22024.
[49] B. Kilic, S. Turkdogan, *Mater. Lett.* **2017**, *193*, 195–198.
[50] a) L. Chang, Y. H. Hu, *J. Phys. Chem. Solids* **2018**, *116*, 347–352; b) S. Kim, O. Dovjuu, S.-H. Choi, H. jeong, J.-T- Park, *Coating* **2019**, *9* 250; c) W. Wei, L. Chang, K. Sun, A. J. Pak, E. Paek, G. S. Hwang, Y. H. Hu, *Nano Lett.* **2016**, *16*, 8029–8033.

[51] F. Tristán-López, D. Ramírez-González, D. A. Cullen, D. J. Smith, M. Terrones, Y. I. Vega-Cantú, *Nano Lett.* **2009**, *9*, 1527–1533.
[52] Z. Salmi, L. Koefoed, B. B. E. Jensen, A. G. Cabo, P. Hofmann, S. U. Pedersen, K. Daasbjerg, *ChemElectroChem* **2016**, *3*, 2202–2211.
[53] G. Maurin, Ch. Bousquet, F. Henn, P. Bernier, R. Almairac, B. Simon, *Chem. Phys. Lett.* **1999**, *312*, 14–18.
[54] E. Frackowiak, F. Béguin, *Carbon* **2002**, *40*, 1775–1787.
[55] L. G. Bulusheva, A. V. Okotrub, A. G. Kurenya, H. Zhang, H. Zhang, X. Chen, H. Song, *Carbon* **2011**, *49*, 4013–4023.
[56] R. Kumar, B. R. Mehta, M. Bhatnagar, S. Ravi, S. Mahapatra, S. Salkalachen, P. Jhawar, *Nanoscale Res. Lett.* **2014**, *9*, 349.
[57] Y. Hao, Y. Wang, L. Wang, Z. Ni, Z. Wang, R. Wang, C. K. Koo, Z. Shen, J. T. L. Thong, *Small* **2010**, *6*, 195–200.
[58] M. L. Hupfer, F. Herrmann-Westendorf, M. Kaufmann, D. Weiß, R. Beckert, B. Dietzek, M. Presselt, *Chem. Eur. J.* **2019**, *25*, 1–6.
[59] M. Presselt, F. Herrmann, S. Shokhovets, H. Hoppe, E. Runge, G. Gobsch, *Chem. Phys. Lett.* **2012**, *542*, 70–73.

Manuscript received: July 22, 2019
Revised manuscript received: November 1, 2019
Version of record online: December 4, 2019